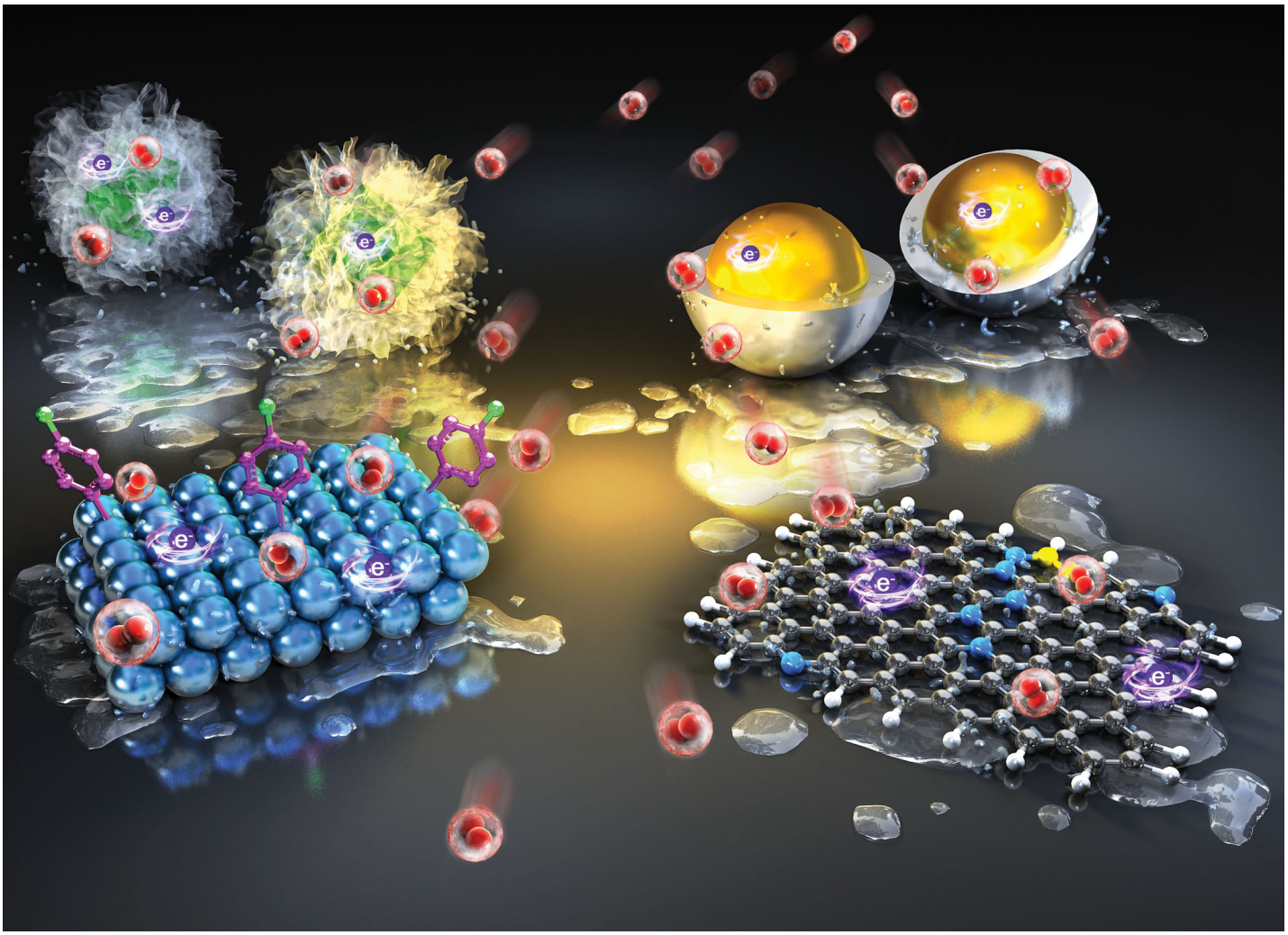

Showcasing collaborative work from the laboratory of Prof. Shaowei Chen at the Department of Chemistry and Biochemistry, University of California at Santa Cruz, and Prof. Ligui Li at New Energy Research Institute, School of Environment and Energy, South China University of Technology.

Impacts of interfacial charge transfer on nanoparticle electrocatalytic activity towards oxygen reduction

In this review article we summarize recent advances in the deliberate manipulation of interfacial charge transfer of metal (alloy) nanoparticles, organically capped metal nanoparticles, metal–carbon composite nanoparticles, and heteroatom doped graphitic carbons, and their impact on the electrocatalytic activity towards the oxygen reduction reaction (ORR), a critical process at fuel cell cathodes. This is of fundamental significance in the rational design of effective ORR electrocatalysts and optimization of their catalytic activity.

As featured in:

See Ligui Li, Shaowei Chen *et al.*, *Phys. Chem. Chem. Phys.*, 2017, **19**, 9336.

ROYAL SOCIETY OF CHEMISTRY

rsc.li/pccp

Registered charity number: 207890

PCCP

PERSPECTIVE

View Article Online
View Journal | View Issue

Cite this: *Phys. Chem. Chem. Phys.*, 2017, **19**, 9336

Impacts of interfacial charge transfer on nanoparticle electrocatalytic activity towards oxygen reduction

Yi Peng,†[a] Bingzhang Lu,†[a] Nan Wang,[b] Ligui Li*[b] and Shaowei Chen*[ab]

Polymer electrolyte membrane fuel cells represent a next-generation power supply technology that may be used in a diverse range of applications. Towards this end, the rational design and engineering of functional nanomaterials as low-cost, high-performance catalysts is of critical significance in the wide-spread commercialization of fuel cell technology. One major bottleneck is the oxygen reduction reaction (ORR) at the cathode. Whereas platinum-based nanoparticles have been used as the catalysts of choice, further engineering of the nanoparticles is urgently needed to enhance the catalytic performance and concurrently reduce the costs. Extensive research has also been extended to non-platinum metals or even metal-free nanocatalysts that may be viable alternatives to platinum. In this review article, we will summarize recent progress in these areas of research within the context of interfacial electron transfer: (a) interactions between metal elements in alloy nanoparticles, (b) metal–ligand interfacial bonding interactions, (c) metal–carbon substrate interactions, and (d) heteroatom doping of graphitic carbons. Results have shown that ready manipulation of the electronic interactions between the catalyst surface and oxygen species may serve as a fundamental mechanism for the optimization of the catalytic performance.

Received 30th December 2016,
Accepted 24th January 2017

DOI: 10.1039/c6cp08925a

rsc.li/pccp

Introduction

The development of renewable and sustainable energy technologies has been attracting a great deal of attention.[1–6] Among these, polymer electrolyte membrane fuel cells (PEMFCs) have been proposed as a next-generation power supply technology by converting chemical energy in small organic fuel molecules into electricity at high efficiency.[7] To produce sufficiently high current density for practical applications, catalysts are generally needed for the oxidation of fuel molecules at the anode and the oxygen reduction reaction (ORR) at the cathode. Of these, the ORR has been recognized as a major bottleneck that limits the fuel cell performance, primarily because of its complex reaction pathways and sluggish electron-transfer kinetics. There are two leading pathways for the ORR, the direct pathway where oxygen undergoes four-electron reduction to H_2O and the indirect pathway where peroxide species are produced as an intermediate.[8] Platinum-based nanoparticles have been used extensively as the catalysts of choice for the ORR. However, the wide-spread application of Pt as an ORR electrocatalyst has been hampered by its low natural abundance, high cost, and poor long-term durability.[9,10] To mitigate these issues, extensive research efforts have been devoted to engineering the platinum nanoparticle catalysts for enhanced performance as well as to the development of non-platinum or even metal-free electrocatalysts with comparable ORR activity and low costs.[11–23]

Mechanically, the ORR entails multiple reaction steps, and in acid media, the reaction pathway is summarized below,

$$* + O_2 + H^+ + e^- \rightarrow OOH* \quad (1)$$

$$OOH* + H^+ + e^- \rightarrow O* + H_2O \quad (2)$$

$$O* + H^+ + e^- \rightarrow OH* \quad (3)$$

$$OH* + H^+ + e^- \rightarrow H_2O + * \quad (4)$$

where * denotes catalyst surface active sites. It has been found that the first-electron reduction of oxygen (eqn (1)) forming OOH* and the final reduction of OH* to water (eqn (4)) are the likely rate-determining steps, due to an uphill energy change in both steps, as suggested in theoretical studies. According to the so-called "volcano plot" (Fig. 1a),[24,25] for optimal ORR activity, the bonding of oxygen species to the electrocatalyst surface cannot be too strong or too weak. This may be correlated with

[a] *Department of Chemistry and Biochemistry, University of California, 1156 High Street, Santa Cruz, California 95064, USA. E-mail: Shaowei@ucsc.edu*
[b] *New Energy Research Institute, School of Environment and Energy, South China University of Technology, Guangzhou Higher Education Mega Center, Guangzhou 510006, China. E-mail: esguili@scut.edu.cn*
† These authors contributed equally to this work.

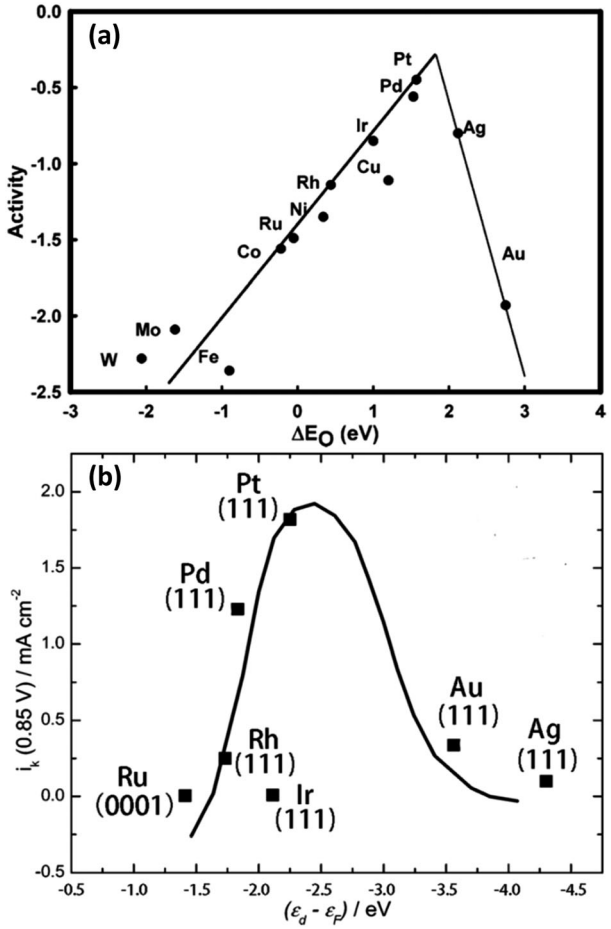

Fig. 1 (a) Trends in the oxygen reduction reaction activity plotted as a function of the oxygen binding energy. The activity is defined as $A = kT\min_i(\log(k_i/k_0))$. (b) Kinetic currents ($j_k$) at +0.80 V *vs.* RHE for the ORR on different metal single crystals in 0.1 M NaOH solution as a function of the calculated metal d-band center (e_d–e_f; relative to the Fermi level). (a) Reproduced with permission from ref. 24, copyright 2004 American Chemical Society. (b) Reproduced with permission from ref. 26, copyright 2007 American Chemical Society.

the d-band center of the electronic structure of the electrocatalyst surface relative to the Fermi level (Fig. 1b).[26] The ORR activity of Pt is predicted to be the best among the series of transition metals. Yet, to reach the peak performance, the binding energy of oxygen species to Pt needs to be weakened by 0.1–0.2 eV. In fact, in order to enhance the ORR activity of the catalysts located on the left side of the volcano plot, the binding energy to oxygen species must be diminished, while for the ones located on the right side (*e.g.*, Ag and Au), the binding should be strengthened. Traditionally, this may be achieved by a number of strategies such as manipulation of nanoparticle size, shape, metal compositions, *etc.*[9,27–40]

More recently, it has been found that interfacial charge transfer between metal nanoparticles and surface capping ligands or supporting substrates may be exploited as an effective variable in manipulating the electronic energy structure of the nanoparticles and hence the bonding interactions with oxygen species, leading to ready control of the ORR activity. Thus, in this perspective article, we will summarize recent progress in the studies of the impacts of interfacial charge transfer on the nanoparticle ORR activity, with a focus on the following areas: (1) alloy nanoparticles, (2) metal–ligand interfacial bonding interactions, (3) electronic interactions between metal nanoparticles and carbon supports, and (4) heteroatom doping of carbon skeletons.

Charge transfer in alloy nanoparticles

One effective strategy to enhance the ORR performance of platinum catalysts and concurrently reduce the costs is by alloying platinum with a non-noble metal. This has been largely ascribed to the manipulation of the Pt d band center by the added non-noble metal diluents due to electronic and geometrical effects.[12,41–48] For instance, Stamenkovic *et al.*[9] showed that the ORR activity of the $Pt_3Ni(111)$ electrode was about 10 and 90 times higher than that of Pt(111) and state-of-the-art commercial Pt/C catalysts, respectively. Structural characterization showed that Pt was rich in both the outermost and third atomic layers while Ni was rich in the second layer. Such interfacial alloying led to weakened interactions between the surface Pt atoms and oxygenated intermediates, consistent with the prediction by the volcano plot, because of effective charge transfer from Ni to Pt that resulted in a decrease of the Pt d band center.[24,25,49,50] As depicted in Fig. 2, the d-band center was estimated to be −3.14 eV on $Pt_3Ni(100)$, −3.10 eV on $Pt_3Ni(111)$ and −2.70 eV on $Pt_3Ni(100)$, all lower than those of Pt, −2.90 eV on Pt(100), −2.76 eV on Pt(111), and −2.54 eV on Pt(110).[51,52]

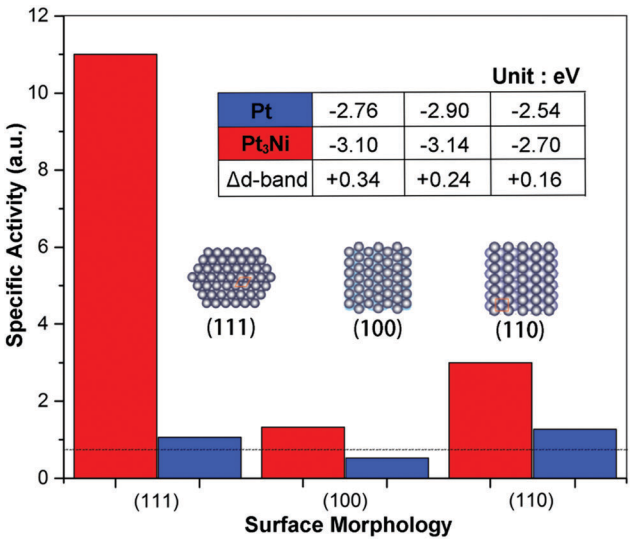

Fig. 2 Influence of surface morphology and electronic surface properties on ORR kinetics. The specific activity (kinetic current densities) of ORR on $Pt_3Ni(hkl)$ surfaces compared with the corresponding Pt(*hkl*) surfaces is shown and is derived from rotation ring disk electrode (RRDE) measurements in 0.1 M $HClO_4$ at 333 K at a rotation rate of 1600 rpm at +0.9 V *versus* RHE (reversible hydrogen electrode). The d-band center position of each morphologic surface was obtained from ultraviolet photoemission spectroscopic (UPS) measurements. Adapted with permission from ref. 9, copyright 2007 American Association for the Advancement of Science.

Of these, the (111) facet of the alloyed surface exhibited the largest down-shift of the d-band center and hence the largest enhancement of the ORR activity, with the ORR activity varying in the order of Pt_3Ni (111) ≫ (110) > (100).[53] Such a fundamental mechanism based on the d-band center has indeed been exploited for the design and engineering of a large number of alloy nanoparticles for ORR electrocatalysis.[54–56]

Such intermetallic charge transfer may be enhanced by asymmetrical distribution of the metal components within the nanoparticles. For instance, in recent studies,[57,58] we prepared bimetallic Ag@Au Janus nanoparticles by interfacial engineering,[59,60] as manifested in Fig. 3a, where a glass slide coated with a monolayer of 1-hexanethiolate-passivated silver nanoparticles (AgC6) was immersed into a solution of gold(I)–mercaptopropanediol complex (Au^I–MPD) and bimetallic Janus nanoparticles were produced as the galvanic exchange reaction was limited to the top face of the nanoparticles. The asymmetrical elemental distribution of the Ag@Au Janus nanoparticles was visually evidenced in elemental mapping by energy dispersive X-ray (EDX) analysis, as depicted in Fig. 3b. Interestingly, the bimetallic Ag@Au Janus nanoparticles exhibited an onset potential at +0.917 V, which was more positive than that of homogeneously alloyed AgAu nanoparticles prepared by bulk exchange reactions (+0.809 V) and of the original AgC6 nanoparticles (+0.792 V), based on RRDE measurements in an oxygen-saturated 0.1 M NaOH solution. Also, the average number (n) of electron transfer in oxygen reduction can be estimated to be 2.46, 3.15 and 3.36 for AgC6, bulk-exchange AgAu nanoparticles and Ag@Au Janus nanoparticles, respectively, indicating that oxygen more likely underwent four-electron reduction to OH^- on the Ag@Au Janus nanoparticle surface than on the other two samples. Fig. 3c depicts the Tafel plots of the three nanoparticles and it can be seen that the ORR kinetic current density increased markedly in the order of AgC6 < bulk-exchange AgAu ≪ Ag@Au Janus nanoparticles. This was attributed to the unique charge transfer from Au to Ag in the nanoparticles, as manifested in XPS measurements where the binding energy of the Ag $3d_{5/2}$ electrons was estimated to be 368.00 eV for bulk-exchange AgAu nanoparticles and 368.55 eV for Janus Ag@Au nanoparticles.[61,62] Note that prior studies have shown that the binding energy of the Ag 3d electrons decreases as the Ag oxidation state increases.[63,64]

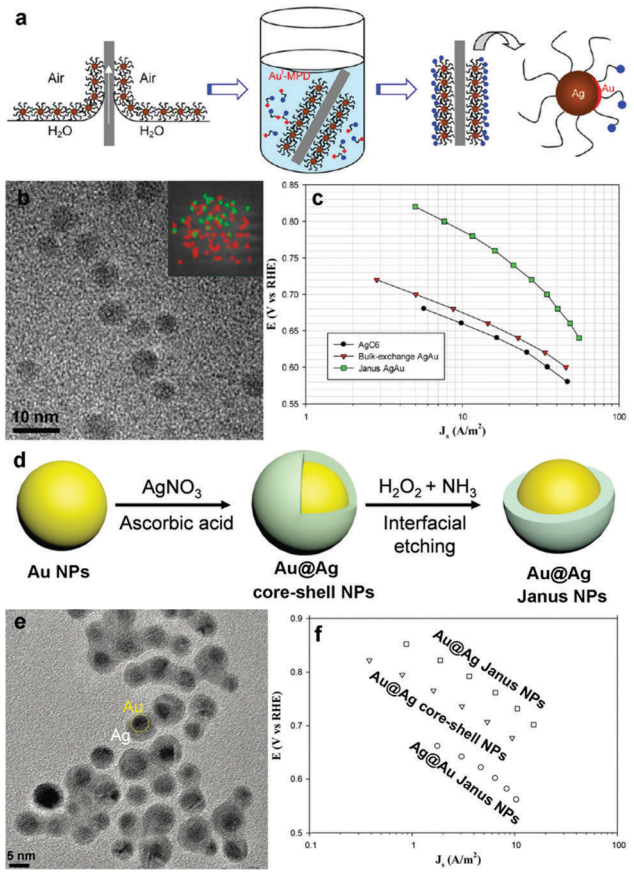

Fig. 3 (a) Schematic of the preparation of Ag@Au bimetallic Janus nanoparticles based on interfacial galvanic exchange reactions of AgC6 nanoparticles with the Au^I–MPD complex. (b) Representative false-color EDS elemental mapping of a Janus nanoparticle with red symbols for Ag and green for Au. (c) Tafel plots of the area-specific kinetic current densities at various electrode potentials. (d) Schematic diagram of the synthesis of Au core@Ag semishell Janus nanoparticles by interfacial etching. (e) Representative TEM images of the Au core@Ag semishell nanoparticles. (f) Tafel plots of the area-specific (open signals) and mass-specific (solid signals) kinetic current densities at various electrode potentials. Panels (a–c) are reproduced with permission from ref. 57, copyright 2012 American Chemical Society, and panels (d–f) are reproduced with permission from ref. 58, copyright 2016 The Royal Society of Chemistry.

Similar effects have also been observed with gold core@silver semishell Janus nanoparticles (Fig. 3d and e), which were prepared by chemical etching of Au@Ag core–shell nanoparticles at the air/water interface by hydrogen peroxide and ammonia.[58] The ORR performance was then evaluated and compared by electrochemical measurements. It can be seen that the Au@Ag semishell Janus nanoparticles exhibited an onset potential of +0.95 V, more positive than that of Au@Ag core–shell nanoparticles (+0.91 V) and Au nanoparticles (+0.77 V). Additionally, the n value at +0.60 V was estimated to be 3.98, 3.92 and 3.53, respectively, suggesting enhanced ORR activity of the alloy nanoparticles as compared to their monometallic Au counterparts, and the semishell Janus nanoparticles stood out as the best among the series. This is also manifested in the Tafel plots (Fig. 3f), where the ORR activity of the Au@Ag semishell Janus nanoparticle was superior to those of Au@Ag and Ag@Au core–shell nanoparticles, monometallic Au or Ag nanoparticles (of similar sizes)[65–67] and even comparable to that of state-of-the-art commercial Pt/C catalysts (except with a lower mass activity).[68] This enhancement was due to a synergistic effect between the gold cores and silver semishells that optimized oxygen binding to the nanoparticle surface due to interfacial charge transfer from Au to Ag.[57] Consistent behaviors have also been observed previously with Au@Ag@Au double shell nanoparticles.[69]

From these examples, one can see that charge transfer between metal components may serve as a powerful parameter in the manipulation of the bonding interactions between metal nanoparticles and oxygen intermediates, and the effects may be further enhanced with Janus nanoparticles as compared to their structurally symmetrical counterparts (*e.g.*, core–shell and homogeneously alloyed nanoparticles).

Metal–ligand interfacial bonding interactions

In recent studies, metal–ligand interfacial bonding interactions have also been found to play an important role in manipulating the bonding interactions of metal nanoparticles with oxygen species and hence the ORR performance.[70] This is somewhat counterintuitive as surface capping ligands will inevitably block part of the surface active sites and compromise the catalytic activity,[10,71–76] such as the poisoning effects of CO or sulfur species.[77–79] Yet recently, it has been found that by deliberate engineering of the nanoparticle surfaces by the formation of covalent metal–ligand interfacial bonding interactions, the electronic density of the metal nanoparticles and hence the interactions with reaction species may be manipulated by the chemical nature of the organic ligands through the geometric effects and charge transfer effects of the capping ligands.[80,81] The former has indeed been exploited for enhanced selectivity of the catalysts[82–84] and as blockers for poisonous species.[85–87] For example, Schrader *et al.* reported that L-proline functionalized Pt nanoparticles of 1.2 nm in diameter exhibited high stereoselectivity in the hydrogenation of ethylacetoacetate with a 34% enantiomeric excess of ethyl(*R*)-3-hydroxybutyrate.[84] Genorio *et al.* demonstrated that chemical modification of a Pt electrode surface with a self-assembled monolayer of calix[4]arene effectively suppressed the ORR while the hydrogen oxidation reaction was allowed to proceed.[86]

More interestingly, with the formation of covalent metal–ligand interfacial bonds, charge transfer may take place across the interface, leading to ready control of the electronic structures of the nanoparticle catalysts.[88] For instance, Chung *et al.* observed a much better ORR activity with oleylamine-capped platinum (Pt_OA) catalysts than the unmodified ones and claimed the enhancement was due to the downshift of the frontier d-band structure of Pt,[87,89] in contrast to earlier results where removal of the oleylamine ligands was found to enhance the catalytic performance.[90,91] As highlighted in Fig. 4a, the electrochemical surface area (ECSA) calculated by underpotential deposition of hydrogen decreased with increasing oleylamine surface coverage. However, Pt_OA exhibited higher onset potentials than the unmodified Pt one (Fig. 4b). Synchrotron-based photoelectron spectroscopy (PES)[92,93] and extended X-ray absorption fine structure spectroscopy (EXAFS) studies were then carried out to characterize the d-band structures of the electrocatalysts. PES measurements suggested that the adsorption of oleylamine ligands lowered the d-band center of Pt_OA as compared to that of unmodified Pt, and the downshift of the d-band center was proportional to the capping ligand surface coverage.[50,94,95] This change was also confirmed by EXAFS measurements.[96] The downshift of the d-band center occurred by increasing electron density in the frontier d states of Pt and may be related to the geometric effect and/or electronic effect. The EXAFS measurements also showed that the Pt–Pt distance (*R*-spacing) remained unchanged after oleylamine modification, indicating that the enhancement was not caused by the geometric effect.[97] Fig. 4c further correlates the enhancement of the ORR activity (kinetic current densities

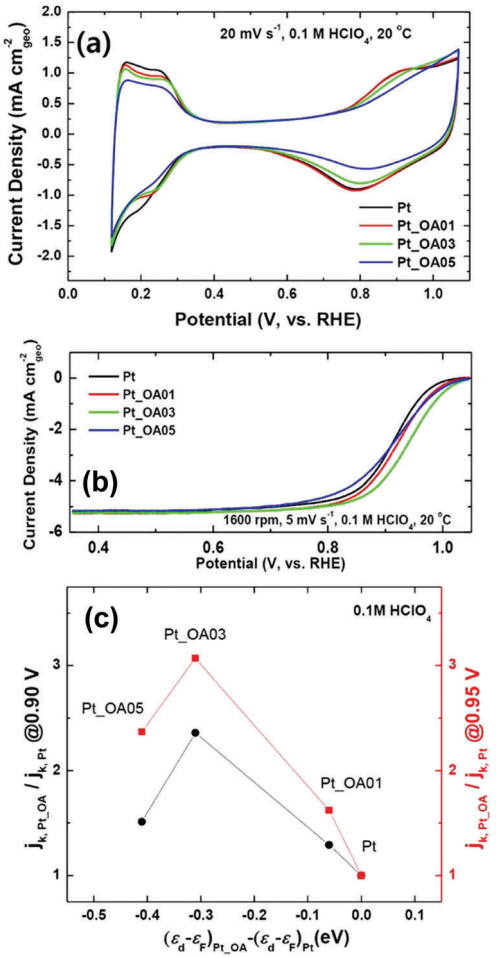

Fig. 4 (a) Cyclic voltammograms of Pt nanoparticles modified with different amounts of OA (Pt_OA) and Pt/C in nitrogen-saturated 0.1 M $HClO_4$ at a scan rate of 20 mV s^{-1}. (b) Polarization curves of RDE measurements of Pt_OA and Pt/C in oxygen-saturated 0.1 M $HClO_4$ at a scan rate of 5 mV s^{-1} and a rotating rate of 1600 rpm. (c) Improvement factors ($j_{k,Pt\_OA}/j_{k,Pt}$) compared to Pt/C as a function of the difference of the d-band center, $\Delta\varepsilon_d$, $(\varepsilon_d - \varepsilon_F)_{Pt\_OA} - (\varepsilon_d - \varepsilon_F)_{Pt}$, in 0.1 M $HClO_4$. Reproduced with permission from ref. 89, copyright 2013 American Chemical Society.

at +0.95 V *vs.* RHE) as compared to that of the unmodified Pt and the change of the d-band center, which exhibited a volcano-shaped variation. Other surface capping ligands with an amine end group such as aniline and hexamethylenediamine also showed similar enhancement of the ORR activity, as compared to their unmodified Pt counterparts, implying that the enhancement was indeed caused by the amine end group as it acted as an electron donor.[98]

Recently, a wide range of metal–ligand interfacial bonds have been exploited for nanoparticle surface functionalization.[70] For instance, metal nanoparticles of ruthenium, palladium and platinum, as well as semiconductor nanoparticles such as silicon and titanium dioxide have been functionalized with aryl fragments and acetylene derivatives, and intraparticle charge delocalization may occur with the formation of conjugated core–ligand interfacial bonds, leading to the emergence of new optical and electronic properties.[62,99–112] For instance, we functionalized Pt nanoparticles with phenyl derivatives and observed an apparent

Table 1 Summary of the ORR performance of Pt-Ar-R nanoparticles and Pt/C[a]

Substituent (R)	CH_3	F	Cl	OCF_3	CF_3	Pt/C
σ	−0.017	+0.05	+0.23	+0.35	+0.54	
Particle size (nm)	2.1	2.1	1.85	2.5	2.2	3.3
Specific ECSA ($m^2\ g^{-1}$ Pt)	54	54	93	47	59	80
j_k (mA cm^{-2}) at +0.9 V	0.15	0.30	0.47	0.52	0.65	0.20
j_k (mA mg^{-1}) at +0.9 V	0.082	0.162	0.437	0.244	0.384	0.16

[a] Adapted with permission from ref. 104, copyright 2012 American Chemical Society.

variation of the ORR activities with the electron withdrawing properties of the *para*-substituents (R = $-CH_3$, –F, –Cl, $-OCF_3$, and $-CF_3$).[103,104] The results are summarized in Table 1 and Fig. 5a, where the kinetic current density (j_k) at +0.9 V was correlated with the Hammett substituent constant (σ) that quantitatively describes the electron-withdrawing capacity of the substituent groups on the phenyl ring including both the resonance effect and inductive effect.[113,114] As shown in Fig. 5b, one can see that the ORR performance of $PtArCH_3$ was lower than that of commercial Pt/C while $PtArCF_3$ was ~3 times better than commercial Pt/C. In fact, the ORR performance was found to increase with increasing σ values suggesting that electron-withdrawing substituent groups enhanced the electrocatalytic activity for the ORR in the order of $-CH_3 < -F < -Cl < -OCF_3 < -CF_3$. This may be accounted for by the diminishment of the electron density of Pt surface atoms by the electron-withdrawing substituent groups, leading to a decrease of the binding energy with oxygen species and hence enhanced ORR performance.

Such electron-withdrawing effects of the substituents have indeed been confirmed by FTIR measurements. As the surface capping ligands were strongly attached onto the Pt nanoparticle surface through Pt–C covalent bonds, the strong electronic interactions between the aromatic rings and Pt resulted in an apparent red shift and broadening of the aromatic ring skeleton vibrations. Such a strategy has also been extended to other metal nanoparticles such as Pd and Ru, and for other electrocatalytic reactions like formic acid oxidation.[115,116]

Acetylene derivatives represent another type of capping ligand for nanoparticle surface functionalization and engineering.[106,108,117] In one study,[106] Pt nanoparticles were prepared and capped with 1-decyne (HC10), 4-ethynylphenylacetylene (EPA) and 4-*tert*-butylphenylacetylene (BPA). Electrochemical measurements showed that the ECSAs were 22.8, 21.0 and 8.1 $m^2\ g_{Pt}^{-1}$ for PtHC10, PtEPA, and PtBPA, respectively, markedly lower than that of commercial Pt/C (61.5 $m^2\ g_{Pt}^{-1}$), suggesting limited removal of the capping ligands during the electrochemical activation process. Nevertheless, the onset potential of these samples was estimated to be +0.067, +0.077, and +0.046 V *vs.* Hg/HgO for PtHC10, PtEPA, and PtBPA, respectively, more positive than that (+0.026 V) of commercial Pt/C, and PtEPA was the most active one among the series. The enhancement of the ORR activity was attributed to the optimization of the Pt core electronic structure by the extensive intraparticle charge delocalization between the acetylene moieties, which was manifested in FTIR and photoluminescence measurements.[99–101]

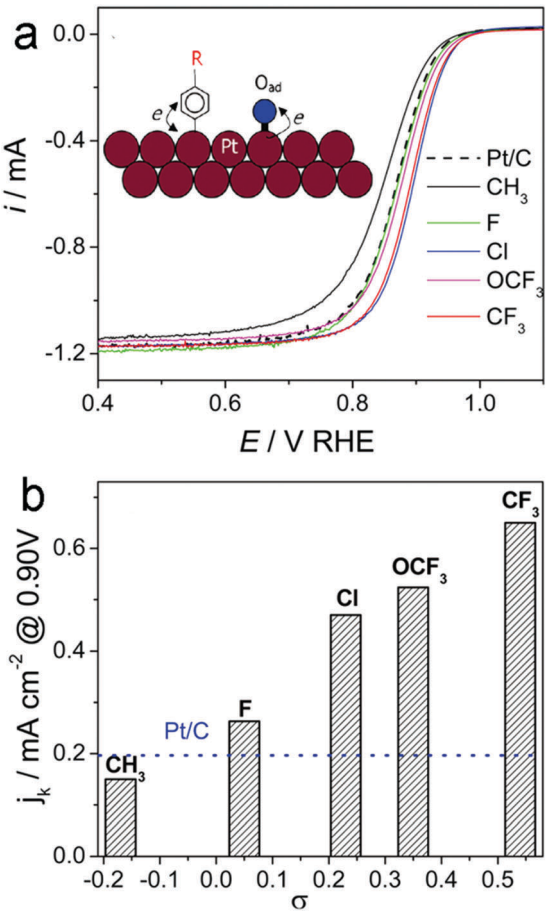

Fig. 5 (a) ORR polarization curves of the Pt–Ar–R nanoparticles and commercial Pt/C catalysts in an O_2-saturated 0.1 M $HClO_4$ solution at room temperature. Electrode rotating rate 1600 rpm; potential scan rate 10 mV s^{-1}. (b) Variation of the ORR specific activity (j_k at +0.90 V) with a Hammett substituent constant (σ). Blue dotted line denotes the ORR activity of commercial Pt/C catalysts. Reproduced with permission from ref. 104, copyright 2012 American Chemical Society.

Olefin derivatives may also be used as capping ligands for nanoparticle surface functionalization, due to interfacial dehydrogenation catalyzed by the metal nanoparticles such that the resulting acetylene moieties self-assemble onto the nanoparticle surface.[108] In a follow-up study with styrene derivatives,[118] we observed drastic impacts of the *para*-substituents on the interfacial reactivity of the ligands and the resulting nanoparticle optical and electronic properties. Experimentally, three styrene derivatives were used, 4-*tert*-butylstyrene (TBS), 4-methoxystyrene (MOS) and 4-(trifluoromethyl)styrene (TFMS). Whereas all three ligands underwent hydrogenation and were bound onto Pt nanoparticles' surfaces forming platinum–vinylidene (Pt═C═C) interfacial bonds,[108,118] the HOMO–LUMO band-gap of the particle-bound acetylene derivatives was found to increase in the order of PtMOS (1.3 ± 0.2 nm) < PtTBS (2.0 ± 0.3 nm) < PtTFMS (1.1 ± 0.2 nm), due to the increasing electron-withdrawing properties of the *para*-substituent groups,[119–122] consistent with the Hammett constant (σ) of methoxy (−0.27) < *tert*-butyl

(−0.20) < trifluoromethyl (+0.54).[113,114] However, the specific activity for the ORR was found to increase in the order of PtMOS < PtTFMS < PtTBS, due to an optimal combination of nanoparticle core size and ligand effects on the bonding interactions between platinum and oxygen species. This mechanism has also been exploited for the optimization of the ORR activity of other metal nanoparticles.[68,105,123,124]

Charge transfer between metal nanoparticles and carbon based supporting substrates

Carbon-based materials have been used extensively as supporting substrates for the dispersion of metal nanoparticle catalysts, and the ORR activity has been found to be readily manipulated by the electronic interactions between the carbon substrates and metal nanoparticles. For instance, in an early study,[125] we prepared 2.8 nm graphene quantum dots (GQDs) by chemical exfoliation of the nanometer-sized sp^2 domains in pitch carbon fibers and deposited Pt nanoparticles on GQDs by a hydrothermal procedure (Fig. 6). The resulting Pt/GQD nanocomposites showed a remarkable ORR activity, with an onset potential at +1.05 V *vs.* RHE in 0.1 M $HClO_4$, which is about 70 mV more positive than that of commercial Pt/C. In addition, the kinetic current density at +0.9 V was about 10 times more than that of commercial Pt/C. This outstanding improvement

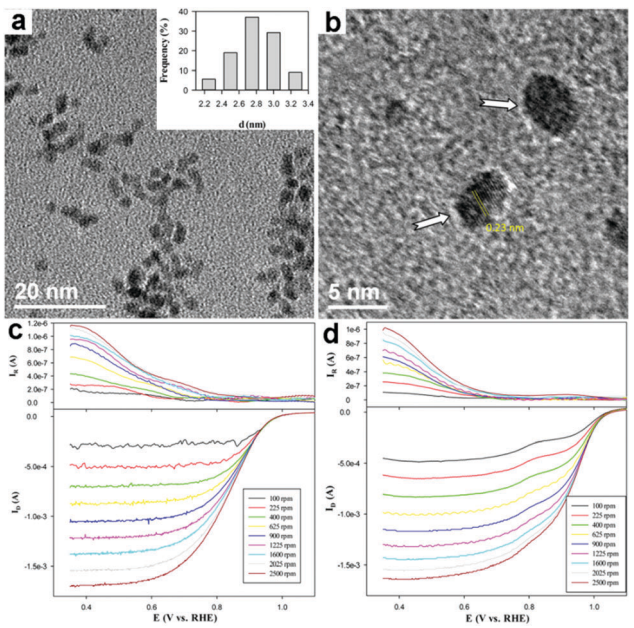

Fig. 6 (a and b) Representative TEM images of GQD-supported Pt nanoparticles. Scale bar is 20 nm in panel (a) and 5 nm in panel (b). Inset in panel (a) shows the nanoparticle core size histogram. Yellow lines in panel (b) highlight the lattice fringes, and white arrows indicate the halos surrounding the Pt nanoparticles. (c and d) RRDE voltammograms of a glassy carbon electrode loaded with (c) Pt/C or (d) Pt/GQD nanoparticle catalysts in an oxygen-saturated 0.1 M $HClO_4$ solution with a scan rate of 5 mV s^{-1}. Ring potential was set at +1.5 V. Reproduced with permission from ref. 125, copyright 2013 American Chemical Society.

was attributed to the GQD structural defects (primarily oxygenated species) that induced electron transfer from the Pt nanoparticles,[8] leading to reduced electron density of the Pt nanoparticles, analogous to the capping ligand effects observed in Fig. 5. In a follow-up study,[126] the GQD defect concentration was manipulated by hydrothermal treatment at controlled temperatures (140–200 °C) for a varied period of time, and the ORR activity was found to reach a maximum at *ca.* 20% structural defects, as quantified by XPS and Raman measurements.

Nanocomposites with other metals such as Cu[127] and Pd[128] were also prepared in a similar fashion. Yet because the binding to oxygen increased in the order of Pt < Pd < Cu, according to the volcano plot, the optimal defect concentration increased accordingly, at *ca.* 50% for Pd/GQDs and 63% for Cu/GQDs. Nonetheless, one may notice that such a high level of structural defects likely compromises the composite electrical conductivity and hence the eventual ORR performance. This issue may be mitigated by using heteroatom-doped GQDs, as the dopants are embedded within the graphitic molecular skeleton and known to actually enhance the electrical conductivity; concurrently the dopants may serve as additional structural defects in manipulating the nanoparticle electronic density. This has indeed been observed in a recent study with Pd nanoparticles supported on nitrogen-doped graphene quantum dots (Pd/NGQDs).[129] XPS measurements showed that nitrogen was embedded within the graphitic molecular skeleton only in the pyridinic and pyrrolic configurations (both p-type doping) and the total concentration remained almost invariant during hydrothermal reactions at 160 °C for up to 12 h. Yet, the fraction of pyrrolic nitrogen was found to increase with prolonging the hydrothermal reaction time, and concurrently a diminishment was observed with the pyridinic N, suggesting a conversion of pyridinic N to pyrrolic N during the hydrothermal reaction. Because the five-member ring pyrrolic N is more defective than the six-member ring pyridinic N, the electron transfer from the Pd nanoparticles to the GQD structural defects became more pronounced with the sample featuring a higher concentration of pyrrolic N, as manifested in XPS measurements. Indeed electrochemical measurements showed markedly enhanced ORR activity, as compared with the Pd/GQDs prepared above.[128]

A similar phenomenon was observed by Song *et al.*[130] where Pd nanoparticles of 3 to 6 nm in diameter were dispersed on N-doped mesoporous carbon frameworks (Pd/NMC). The hybrid materials were synthesized first by pyrolysis of knitting aryl network polymers at 800 °C to produce N-doped mesoporous carbon frameworks, onto which Pd nanoparticles were deposited by thermal reduction of palladium precursors in a H_2 flow at 200 °C. XPS measurements showed that the binding energy of Pd was 1.1 to 1.3 eV higher than the standard value, indicating diminished electron density on Pd due to strong interactions between Pd and the carbon support. The shift was markedly lower at only *ca.* 0.2 eV with nitrogen-free carbon frameworks, suggesting that nitrogen dopants played a significant role in interfacial electron transfer. Voltammetric tests showed that the Pd/NMC composites indeed exhibited a

remarkable ORR performance, where the onset potential was much higher than that of commercial Pd/C, and the half-wave potential was even 25 mV more positive than that of Pt/C.

Carbon materials can not only improve the catalytic activity, but enhance the durability as well. For instance, Guo *et al.*[131] used carbon nanotubes as templates to synthesize 1D polyaniline. By high-temperature carbonization and deposition, they successfully prepared Pt nanoparticles on the resulting porous N-doped carbon nanotubes (the sample was denoted as Pt–CN_x/CNT). XPS measurements showed an obvious positive shift (*ca.* 0.76 eV) of the binding energy of the Pt $4f_{5/2}$ and $4f_{3/2}$ electrons in Pt–CN_x/CNT as compared to Pt/C, and a negative shift of the N 1s binding energy of graphitic N in the sample. This indicated electron transfer from Pt to N doped carbon. Durability tests showed that the ORR specific activity and mass activity of Pt–CN_x/CNT at +0.85 V *vs.* RHE remained almost unchanged, at *ca.* 1.5 A m^{-2} and 110 A g^{-1}, respectively, in contrast to commercial Pt/C which exhibited a significant decrease from 1.25 to 0.88 A m^{-2} and 110 to 27.5 A g^{-1}, respectively.

Different from Pt and Pd based catalysts, Au is located on the other side of the volcano plot.[49] Thus, a different electron-transfer behavior will have to be used in order to increase the ORR activity. In recent studies,[22,132] we synthesized gold nanoparticles of 3 to 6 nm in diameter on porous carbons (Au/PC) by high-temperature pyrolysis of the mixture of $Au_x(SC_2H_4Ph)_y$ precursors and porous carbon. XPS studies showed that the binding energy of the Au $4f_{5/2}$ and $4f_{7/2}$ electrons were identified at 88.0 and 84.4 eV for the unsupported nanoparticles, but lower for the Au/PC hybrids at 87.8 and 84.0 eV. This was accounted for by electron transfer from the carboxylic/carbonyl moieties to gold, which increased the electron density of gold and hence the binding interactions with oxygen species, leading to enhanced ORR performance. For instance, the onset potential was estimated to be +0.95 V *vs.* RHE, comparable to that of commercial Pt/C catalysts.

In another recent study,[133] we designed and synthesized a hybrid material (Au@Zn–Fe–C) consisting of single Au nanoparticles encapsulated in a Zn,Fe-codoped carbon shell as dual catalysts for the ORR and HER (hydrogen evolution reaction). Experimentally, Zn,Fe-embedded porous carbon (Zn–Fe–C) was prepared by thermal treatment of $Fe(acac)_3$, $Zn(NO_3)_2$, and 1,4-benzenedicarboxylic acid, whereas gold nanoparticles were synthesized by hydrothermal reduction of $HAuCl_4$ in DMF–ethanol (v : v 5 : 3). These two samples were then mixed at controlled loadings and underwent pyrolysis at elevated temperatures, affording Au@Zn–Fe–C egg@yolk nanocomposites, as shown in Fig. 7a–e, with a single gold nanoparticle of 50–100 nm in diameter encapsulated in a 30–60 nm porous carbon shell embedded with Zn–Fe compounds. In XPS measurements (Fig. 7f) the Au $4f_{7/2}$ and Au $4f_{5/2}$ electrons exhibited a binding energy of 84.2 and 88.0 eV, a positive shift of *ca.* 1.4 eV as compared to that of pure Au nanoparticles (82.8 and 86.6 eV). This indicated a strong electron transfer from the Au core to the Zn–Fe–C shell where the catalytic reactions occurred. Electrochemically, the onset potential for the ORR was identified

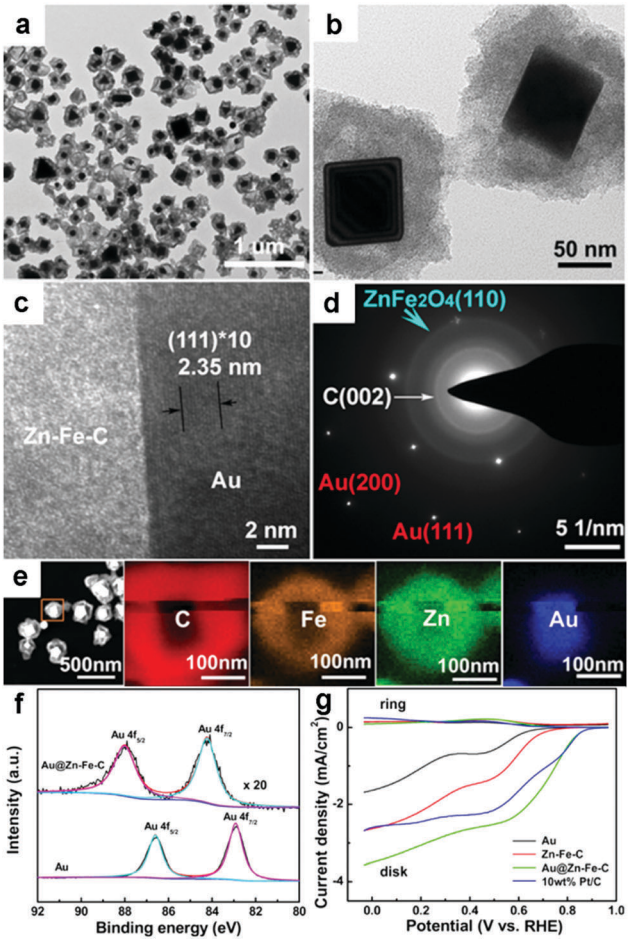

Fig. 7 (a and b) Representative TEM, (c) HRTEM images, (d) the corresponding SAED patterns, and (e) EDX maps of Au@Zn–Fe–C hybrids. (f) High-resolution XPS scans of Au 4f electrons of the Au@Zn–Fe–C hybrids and pure Au nanoparticles. (g) RRDE voltammograms of Au nanoparticles, Zn–Fe–C, Au@Zn–Fe–C, and 10 wt% Pt/C at a rotation rate of 1600 rpm in an O_2-saturated 0.1 M KOH solution at 10 mV s^{-1}. Reproduced with permission from ref. 133, copyright 2016 American Chemical Society.

at +0.94 V *vs.* RHE for Au@Zn–Fe–C, markedly more positive than that of Zn–Fe–C (+0.84 V) and gold nanoparticles (+0.80 V) alone.

In summary, these studies highlight the fundamental significance of electron transfer at the metal–carbon interface in manipulating the electronic interactions with reaction species and the eventual electrocatalytic performance.

Charge transfer in heteroatom-doped carbons

Heteroatom-doped (N, B, P, S, *etc.*) carbons have also emerged as promising metal-free catalysts for the ORR due to their remarkable ORR activity along with the wide availability of their source materials, and their low costs, high conductivity, chemical inertness, and environmental friendliness. Mechanistically, Xia *et al.*[134] proposed that the ORR catalytic active sites on N-doped graphene are significantly influenced by the

electron spin density distribution and atomic charge distribution. Generally, the carbon atoms that have the highest electron spin density are considered to be the active sites. If the negative value of the electron spin density is small, then the carbon atoms with a high density of positive charges may act as the active sites. DFT calculations show that any chemical species presented in the form of either elemental substitution or attachment on graphene can also lead to a high asymmetric electron spin density and atomic charge density on graphene, and hence promote the ORR, which is consistent with the results in a series of studies (*vide infra*). However, it is not yet clear which nitrogen dopant is responsible for the ORR activity because there are at least three kinds of nitrogen doping configurations in the molecular skeletons of graphene, *i.e.*, pyrrolic N, pyridinic N and graphitic N. For instance, Wei *et al.*[135] proposed that the electrocatalytically active sites were carbon atoms adjacent to both (p-type) pyridinic and pyrrolic N. In contrast, recently Nakamura *et al.*[136] suggested that the ORR active sites were carbon atoms directly bonded to pyridinic N alone after a systematic study of the ORR activity of N-doped highly oriented pyrolytic graphite (HOPG). More recently, Dai and co-workers[137] claimed that (n-type) graphitic N was actually responsible for the catalytic activity of the ORR in N-doped graphene nanoribbon networks.

In another study,[138] Jung *et al.* carried out DFT calculations and found that the graphitic-N site on the edge of graphene (N0, Fig. 8a) possessed the most desirable characteristics, *i.e.*, the lowest barrier for the rate-limiting first electron transfer as well as the highest selectivity toward the four-electron reduction pathway among the graphitic nitrogen at various positions, and hence this was proposed to be the main active site for the ORR. Interestingly, they also found the transformation of graphitic N on the edge to pyridinic-like nitrogen in the second electron and concurrently proton transfer reaction *via* the ring-opening of a cyclic C–N bond, and proposed a mechanism for the ORR in N-doped carbons as shown in Fig. 8b.

Despite the progress, the identification of the ORR active sites has remained a matter of active debate. There are three major issues. The first one is the structural complexity where all three nitrogen doping configurations are generally present in N-doped carbons prepared by, for instance, direct pyrolysis of N-containing carbonaceous precursors or by annealing of graphene derivatives under a NH_3 atmosphere. The second one lies in the heterogeneity within the context of morphology, degree of graphitization, and composition. The third one is the inter-conversion between the various nitrogen dopants, which complicates the discrimination process that correlates the ORR activity with the specific nitrogen dopants.

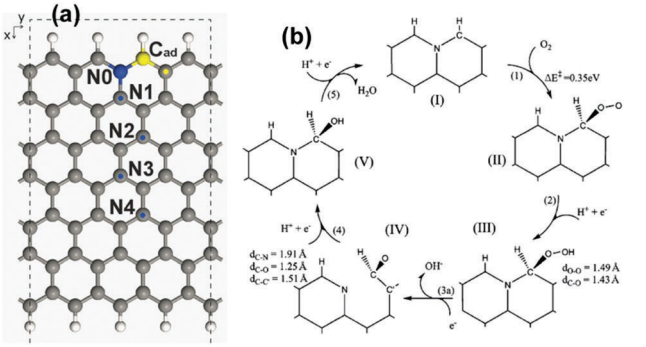

Fig. 8 (a) A model structure showing various graphitic nitrogen geometries. The oxygen molecule is adsorbed at C_{ad} (yellow atom). The nitrogen, oxygen and hydrogen atoms are colored blue, red, and white, respectively, and the dotted line denotes a periodic boundary. (b) Proposed ORR catalytic cycle for the N0 site. Adapted with permission from ref. 138, copyright 2016 The Royal Society of Chemistry.

Currently, the ORR activity has been primarily ascribed to two factors.

(a) The edge defects. Shen *et al.*[139] developed and used a microprobe apparatus to track the ORR process in an air-saturated droplet with a diameter of about 15 μm on HOPG. In this study, the HOPG substrate was used as a working electrode, and the air-saturated liquid droplet served as the electrolyte, while an Ag/AgCl wire and a Pt wire integrated in a capillary tube in direct contact with the droplet worked as a reference and counter electrode, respectively. Using this apparatus, they found that the ORR proceeded on the locations with plenty of steps (*i.e.*, edges) and showed a more positive onset potential together with a much higher current density than on smooth planes of HOPG. This signifies that the edge of the honeycomb-like carbon skeletons in graphene is more active than the basal plane towards the ORR. This conclusion was further supported by the results of control experiments, where substantially enhanced ORR activity was indeed observed on edge-rich graphite powder catalysts prepared by ball-milling of raw graphite powders. In addition, DFT calculations suggested that the presence of higher charge densities on the edge carbon atoms accounted for the improvement of the ORR activity. In non-doped carbons, the charges may originate from the delocalized electrons from basal plane carbon atoms to the edge carbon atoms,[14] resembling a charge transfer process, and the unpaired electrons on the edge play a significant role in ORR electrocatalysis. Edge-rich dopant-free graphene, carbon nanotubes and graphite catalysts have also been prepared by Ar plasma etching, and these edge-rich catalysts show enhanced ORR activity as compared to their untreated counterparts.[130] Recently, by a series of electrochemical and DFT calculations of topological defect-rich nanocarbon prepared by carbonization of natural sticky rice, Tang *et al.*[140] found that the adjacent pentagon and heptagon carbon rings on the edges of nitrogen-free honeycomb-like carbon skeletons exhibited the lowest overpotential for both oxygen reduction and evolution catalysis, confirming that the edges of graphene carbons are highly active in oxygen electrocatalysis.

(b) Breaking of electroneutrality. As mentioned above, whereas edges of graphite contribute to the ORR activity, the ORR activity of these edge-rich dopant-free carbons is normally inferior to that of commercial Pt/C. In graphite materials, most carbon atoms are located in the basal six-carbon rings (6C-ring), far away from the edges. Hence an immediate question arises. How can the inert 6C-ring carbon atoms be transformed into highly active sites for the ORR so that the overall ORR activity of

carbon-based catalysts can be enhanced? Within this context, Gong *et al.*[141] synthesized a vertically-aligned nitrogen-doped carbon nanotube (VA-NCNT) array by pyrolyzing iron(II) phthalocyanine which exhibited a much higher electrocatalytic activity, better long-term stability, and stronger tolerance against the fuel-crossover effect than commercial Pt/C. Quantum mechanics calculations showed a remarkably high density of positive charge on the carbon atoms adjacent to the nitrogen dopants, suggesting part of the electrons were pulled to the nitrogen dopants because nitrogen possessed stronger electron affinity than carbon (Table 2).[142] Such nitrogen dopant-induced charge transfer helped transform the chemisorption mode of O_2 molecules from the usual end-on adsorption configuration (Pauling model) on the non-doped basal plane of CNTs to a side-on fashion (Yeager model) on the N-doped CNTs, which effectively weakened the O–O bond in O_2 molecules and significantly promoted the ORR activity. N-Doping of porous carbons also renders them highly efficient ORR electrocatalysts, as demonstrated in a number of early studies.[143–147] The results suggest that the breaking of electroneutrality may be exploited for the manipulation of the ORR activity of carbon-based catalysts.

Inspired by these breakthroughs, carbon has also been doped with heteroatoms with much stronger electron affinity than nitrogen such as F[148] and Cl.[149] Interestingly, whereas S shows only slightly higher electron affinity than carbon, positive effects on the ORR activity have been observed.[150] These results clearly demonstrate the importance of the tuning of electron density to the electrocatalytic activity of carbons for the ORR.

The formation of a partial charge-transfer state can also be achieved by doping carbon skeletons with elements that have lower electron affinity than carbon. For example, Yang *et al.*[151] synthesized boron-doped CNTs as metal-free electrocatalysts for the ORR, and they observed that the onset and peak potentials of the ORR in an alkaline electrolyte solution shifted positively and the current density increased noticeably with increasing boron content. DFT calculations suggested that the stronger electron affinity of carbon caused partial electron transfer from the boron dopants to carbon, and the resulting positively charged boron dopants facilitated chemisorption of O_2 onto the CNTs; subsequently, part of the π^* electrons in the conjugated matrix were accumulated on the boron dopants and reduced the chemisorbed O_2 molecules with boron serving as a bridge. Similarly, Liu *et al.*[152] observed a remarkable ORR activity, long-term operation stability, and superb tolerance against methanol crossover with a metal-free P-doped graphite layer catalyst in an alkaline aqueous solution.

In addition to the above doping method, the charge state of carbons can also be manipulated by surface coating. For example, Wang *et al.* coated carbon-based catalysts (CNTs and graphene) with positively charged poly(diallyldimethylammonium chloride) (PDDA) as an electron acceptor.[153,154] Raman and XPS measurements suggested partial charge transfer from the carbon catalysts to PDDA, and the resultant positively charged carbon showed a remarkable electrocatalytic activity toward the ORR, with a better fuel selectivity, and stronger resistance to CO poisoning, as well as a longer lifespan than that of the commercial Pt/C catalysts. Enhanced ORR catalytic activity was also observed with the composite of poly(3,4-ethylenedioxythiophene), poly(styrene sulfonate) and reduced graphene oxide.[155]

Table 2 Electron affinity of selected elements

Element	F	Cl	N	S	C	P	B
Electron affinity	3.98	3.16	3.04	2.58	2.55	2.19	2.04

Summary and perspectives

In summary, interfacial electron transfer within the nanoparticle catalysts plays a critical role in the manipulation of the binding interactions between the catalyst active sites and oxygen intermediates, a critical step in the electroreduction of oxygen that occurs at the cathodes of fuel cells and metal–air batteries. This may lead to ready control and eventual optimization of the ORR activity. Research progress in four different ORR catalyst systems is summarized as examples in this review. For metal nanoparticles, this is accounted for within the context of the d-band center. For the transition metals on the left side of the volcano plot, lowering of the d-band center and hence weakened interactions with oxygen species is desired to improve the ORR performance. This may be achieved by alloying with a more electronegative metal where electron transfer occurs to the ORR active centers, deliberate bonding interactions with selected organic ligands where the electron density of the metal particles may be varied by the electron withdrawing properties of the organic ligands, or interfacial interactions with graphene supporting substrates where the structural defects of the graphene substrates induce charge transfer from the metal nanoparticles. Furthermore, for carbon-based metal-free catalysts, whereas the exact mechanism remains elusive thus far, the ORR activity has been proposed to arise from a change of the charge and/or spin distribution of neighboring carbon atoms.

Progress in these earlier studies lays a solid foundation for future research to further enhance the catalytic performance. For precious metals, the catalytic efficiency will be maximized, and the costs will be minimized, by the rational design and preparation of single-atom catalysts, where the binding interactions with reaction intermediates may be manipulated by interfacial electron transfer through close interactions with another metal element, organic capping ligands or supporting substrates. In these catalysts, structural integrity and catalyst durability will be a great challenge. For metal-free carbon-based catalysts, whereas apparent ORR activity has been observed, further improvement has been hampered by the lack of unambiguous identification of the catalytic active sites, due to the complexity of the catalyst structures which renders it difficult to correlate the ORR activity with the structural characteristics. To mitigate such an issue, one effective approach is to have the structures of the carbon catalysts, as well as the dopant configurations, atomically engineered and resolved. This may be

achieved by, for instance, top-down surgical engineering of graphene nanosheets with precise spatial control of heteroatom doping.

Acknowledgements

This work was supported in part by the US National Science Foundation (DMR-1409396) and the National Natural Science Foundation of China (NSFC 21528301).

References

1 J. L. Bredas, E. H. Sargent and G. D. Scholes, *Nat. Mater.*, 2016, **16**, 35–44.
2 S. Chu, Y. Cui and N. Liu, *Nat. Mater.*, 2016, **16**, 16–22.
3 M. A. Green and S. P. Bremner, *Nat. Mater.*, 2016, **16**, 23–34.
4 C. P. Grey and J. M. Tarascon, *Nat. Mater.*, 2016, **16**, 45–56.
5 J. H. Montoya, L. C. Seitz, P. Chakthranont, A. Vojvodic, T. F. Jaramillo and J. K. Norskov, *Nat. Mater.*, 2016, **16**, 70–81.
6 V. R. Stamenkovic, D. Strmcnik, P. P. Lopes and N. M. Markovic, *Nat. Mater.*, 2016, **16**, 57–69.
7 X. Zou and Y. Zhang, *Chem. Soc. Rev.*, 2015, **44**, 5148–5180.
8 D. H. Lim and J. Wilcox, *J. Phys. Chem. C*, 2012, **116**, 3653–3660.
9 V. R. Stamenkovic, B. Fowler, B. S. Mun, G. F. Wang, P. N. Ross, C. A. Lucas and N. M. Markovic, *Science*, 2007, **315**, 493–497.
10 S.-H. Wu, C.-T. Tseng, Y.-S. Lin, C.-H. Lin, Y. Hung and C.-Y. Mou, *J. Mater. Chem.*, 2011, **21**, 789–794.
11 C. Wang, N. M. Marković and V. R. Stamenkovic, *ACS Catal.*, 2012, **2**, 891–898.
12 J. Wu and H. Yang, *Acc. Chem. Res.*, 2013, **46**, 1848–1857.
13 W. Ding, Z. Wei, S. Chen, X. Qi, T. Yang, J. Hu, D. Wang, L.-J. Wan, S. F. Alvi and L. Li, *Angew. Chem., Int. Ed.*, 2013, **52**, 11755–11759.
14 D.-W. Wang and D. Su, *Energy Environ. Sci.*, 2014, **7**, 576–591.
15 J. Liu, E. Li, M. Ruan, P. Song and W. Xu, *Catalysts*, 2015, **5**, 1167–1192.
16 D. Banham, S. Ye, K. Pei, J.-i. Ozaki, T. Kishimoto and Y. Imashiro, *J. Power Sources*, 2015, **285**, 334–348.
17 P. Hu, K. Liu, C. P. Deming and S. Chen, *J. Chem. Technol. Biotechnol.*, 2015, **90**, 2132–2151.
18 Y. Nie, L. Li and Z. Wei, *Chem. Soc. Rev.*, 2015, **44**, 2168–2201.
19 J. Masa, W. Xia, M. Muhler and W. Schuhmann, *Angew. Chem., Int. Ed.*, 2015, **54**, 10102–10120.
20 W. Xia, A. Mahmood, Z. Liang, R. Zou and S. Guo, *Angew. Chem., Int. Ed.*, 2016, **55**, 2650–2676.
21 T. Asefa, *Acc. Chem. Res.*, 2016, **49**, 1873–1883.
22 L. Wang, Z. Tang, W. Yan, H. Yang, Q. Wang and S. Chen, *ACS Appl. Mater. Interfaces*, 2016, **8**, 20635–20641.
23 Z. Xia, L. An, P. Chen and D. Xia, *Adv. Energy Mater.*, 2016, **6**, 1600458.
24 J. K. Nørskov, J. Rossmeisl, A. A. Logadottir, L. Lindqvist, J. R. Kitchin, T. Bligaard and H. Jónsson, *J. Phys. Chem. B*, 2004, **108**, 17886–17892.
25 J. Greeley, I. E. L. Stephens, A. S. Bondarenko, T. P. Johansson, H. A. Hansen, T. F. Jaramillo, J. Rossmeisl, I. Chorkendorff and J. K. Norskov, *Nat. Chem.*, 2009, **1**, 552–556.
26 F. H. B. Lima, J. Zhang, M. H. Shao, K. Sasaki, M. B. Vukmirovic, a. E A Ticianelli and R. R. Adzic, *J. Phys. Chem. C*, 2006, **111**, 404–410.
27 I. E. L. Stephens, A. S. Bondarenko, U. Gronbjerg, J. Rossmeisl and I. Chorkendorff, *Energy Environ. Sci.*, 2012, **5**, 6744–6762.
28 M. K. Carpenter, T. E. Moylan, R. S. Kukreja, M. H. Atwan and M. M. Tessema, *J. Am. Chem. Soc.*, 2012, **134**, 8535–8542.
29 A. Seo, J. Lee, K. Han and H. Kim, *Electrochim. Acta*, 2006, **52**, 1603–1611.
30 I. E. L. Stephens, A. S. Bondarenko, F. J. Perez-Alonso, F. Calle-Vallejo, L. Bech, T. P. Johansson, A. K. Jepsen, R. Frydendal, B. P. Knudsen, J. Rossmeisl and I. Chorkendorff, *J. Am. Chem. Soc.*, 2011, **133**, 5485–5491.
31 J. R. Kitchin, J. K. Norskov, M. A. Barteau and J. G. Chen, *J. Chem. Phys.*, 2004, **120**, 10240–10246.
32 P. Paalanen, B. M. Weckhuysen and M. Sankar, *Catal.: Sci. Technol.*, 2013, **3**, 2869–2880.
33 Y. Liu, L. Zhang, B. G. Willis and W. E. Mustain, *ACS Catal.*, 2015, **5**, 1560–1567.
34 W. J. Zhou, M. Li, O. L. Ding, S. H. Chan, L. Zhang and Y. H. Xue, *Int. J. Hydrogen Energy*, 2014, **39**, 6433–6442.
35 M. H. Shao, A. Peles and K. Shoemaker, *Nano Lett.*, 2011, **11**, 3714–3719.
36 J. W. Kim, B. Lim, H. S. Jang, S. J. Hwang, S. J. Yoo, J. S. Ha, E. A. Cho, T. H. Lim, S. W. Nam and S. K. Kim, *Int. J. Hydrogen Energy*, 2011, **36**, 706–712.
37 D. J. Ham, A. Phuruangrat, S. Thongtem and J. S. Lee, *Chem. Eng. J.*, 2010, **165**, 365–369.
38 J. B. Wu, J. L. Zhang, Z. M. Peng, S. C. Yang, F. T. Wagner and H. Yang, *J. Am. Chem. Soc.*, 2010, **132**, 4984–4985.
39 C. L. Lee, H. P. Chiou, C. M. Syu and C. C. Wu, *Electrochem. Commun.*, 2010, **12**, 1609–1613.
40 M. H. Shao, J. Odell, M. Humbert, T. Y. Yu and Y. N. Xia, *J. Phys. Chem. C*, 2013, **117**, 4172–4180.
41 Y. Xia, Y. Xiong, B. Lim and S. E. Skrabalak, *Angew. Chem., Int. Ed.*, 2009, **48**, 60–103.
42 Z. Quan, Y. Wang and J. Fang, *Acc. Chem. Res.*, 2013, **46**, 191–202.
43 G. J. Leong, M. C. Schulze, M. B. Strand, D. Maloney, S. L. Frisco, H. N. Dinh, B. Pivovar and R. M. Richards, *Appl. Organomet. Chem.*, 2014, **28**, 1–17.
44 H. Zhang, M. Jin and Y. Xia, *Chem. Soc. Rev.*, 2012, **41**, 8035–8049.
45 N. V. Long, Y. Yang, C. Minh Thi, N. V. Minh, Y. Cao and M. Nogami, *Nano Energy*, 2013, **2**, 636–676.

46 N. S. Porter, H. Wu, Z. Quan and J. Fang, *Acc. Chem. Res.*, 2013, **46**, 1867–1877.
47 L. Zhang, Z. Xie and J. Gong, *Chem. Soc. Rev.*, 2016, **45**, 3916–3934.
48 K. D. Gilroy, A. Ruditskiy, H.-C. Peng, D. Qin and Y. Xia, *Chem. Rev.*, 2016, **116**, 10414–10472.
49 J. Greeley, T. F. Jaramillo, J. Bonde, I. B. Chorkendorff and J. K. Norskov, *Nat. Mater.*, 2006, **5**, 909–913.
50 V. Stamenkovic, B. S. Mun, K. J. J. Mayrhofer, P. N. Ross, N. M. Marković, J. Rossmeisl, J. Greeley and J. K. Nørskov, *Angew. Chem., Int. Ed.*, 2006, **118**, 2963–2967.
51 A. Ruban, B. Hammer, P. Stoltze, H. L. Skriver and J. K. Nørskov, *J. Mol. Catal. A: Chem.*, 1997, **115**, 421–429.
52 M. Mavrikakis, B. Hammer and J. K. Nørskov, *Phys. Rev. Lett.*, 1998, **81**, 2819–2822.
53 N. Markovic, *Surf. Sci. Rep.*, 2002, **45**, 117–229.
54 P. Strasser, *Science*, 2015, **349**, 379–380.
55 P. Strasser, *Acc. Chem. Res.*, 2016, **49**, 2658–2668.
56 H. Mistry, A. S. Varela, S. Kühl, P. Strasser and B. R. Cuenya, *Nat. Rev. Mater.*, 2016, **1**, 16009.
57 Y. Song, K. Liu and S. W. Chen, *Langmuir*, 2012, **28**, 17143–17152.
58 L. M. Chen, C. P. Deming, Y. Peng, P. G. Hu, J. Stofan and S. W. Chen, *Nanoscale*, 2016, **8**, 14565–14572.
59 S. Pradhan, L. Xu and S. Chen, *Adv. Funct. Mater.*, 2007, **17**, 2385–2392.
60 S. Pradhan, L. E. Brown, J. P. Konopelski and S. Chen, *J. Nanopart. Res.*, 2009, **11**, 1895–1903.
61 T. Miller, A. Samsavar, G. E. Franklin and T. C. Chiang, *Phys. Rev. Lett.*, 1988, **61**, 1404–1407.
62 B. D. Phebus, Y. Yuan, Y. Song, P. G. Hu, Y. Abdollahian, Q. X. Tong and S. W. Chen, *Phys. Chem. Chem. Phys.*, 2013, **15**, 17647–17653.
63 G. B. Hoflund, Z. F. Hazos and G. N. Salaita, *Phys. Rev. B: Condens. Matter Mater. Phys.*, 2000, **62**, 11126–11133.
64 M. E. Ibele, R. Liu, K. Beiswenger and A. Sen, *J. Mater. Chem.*, 2011, **21**, 14410–14413.
65 F. Mirkhalaf and D. J. Schiffrin, *Langmuir*, 2010, **26**, 14995–15001.
66 L. Tammeveski, H. Erikson, A. Sarapuu, J. Kozlova, P. Ritslaid, V. Sammelselg and K. Tammeveski, *Electrochem. Commun.*, 2012, **20**, 15–18.
67 S. Bhadra, D. Khastgir, N. K. Singha and J. H. Lee, *Prog. Polym. Sci.*, 2009, **34**, 783.
68 P. G. Hu, Y. Song, L. M. Chen and S. W. Chen, *Nanoscale*, 2015, **7**, 9627–9636.
69 D. T. N. Anh, P. Singh, C. Shankar, D. Mott and S. Maenosono, *Appl. Phys. Lett.*, 2011, **99**, 073107.
70 P. G. Hu, L. M. Chen, X. W. Kang and S. W. Chen, *Acc. Chem. Res.*, 2016, **49**, 2251–2260.
71 D. W. Goodman, *Appl. Surf. Sci.*, 1984, **19**, 1–13.
72 J. A. Rodriguez and J. Hrbek, *Acc. Chem. Res.*, 1999, **32**, 719–728.
73 C. A. Stowell and B. A. Korgel, *Nano Lett.*, 2005, **5**, 1203–1207.
74 K. Senevirathne, A. W. Burns, M. E. Bussell and S. L. Brock, *Adv. Funct. Mater.*, 2007, **17**, 3933–3939.
75 F. Bernardi, A. Traverse, L. Olivi, M. C. M. Alves and J. Morais, *J. Phys. Chem. C*, 2011, **115**, 12243–12249.
76 K. Lee, C. Song and M. J. Janik, *Langmuir*, 2012, **28**, 5660–5668.
77 A. S. Arico, S. Srinivasan and V. Antonucci, *Fuel Cells*, 2001, **1**, 133–161.
78 J. J. Baschuk and X. Li, *Int. J. Hydrogen Energy*, 2001, **25**, 695–713.
79 J. A. Rodriguez, *Prog. Surf. Sci.*, 2006, **81**, 141–189.
80 A. Ananthanarayanan, Y. Wang, P. Routh, M. A. Sk, A. Than, M. Lin, J. Zhang, J. Chen, H. Sun and P. Chen, *Nanoscale*, 2015, **7**, 8159–8165.
81 S. Kunz, *Top. Catal.*, 2016, 1–15.
82 S. Kunz, P. Schreiber, M. Ludwig, M. M. Maturi, O. Ackermann, M. Tschurl and U. Heiz, *Phys. Chem. Chem. Phys.*, 2013, **15**, 19253–19261.
83 K. R. Kahsar, D. K. Schwartz and J. W. Medlin, *J. Am. Chem. Soc.*, 2014, **136**, 520–526.
84 I. Schrader, S. Neumann, R. Himstedt, A. Zana, J. Warneke and S. Kunz, *Chem. Commun.*, 2015, **51**, 16221–16224.
85 H. A. Kozlowska, B. MacDougall and B. E. Conway, *J. Electrochem. Soc.*, 1973, **120**, 756–766.
86 B. Genorio, D. Strmcnik, R. Subbaraman, D. Tripkovic, G. Karapetrov, V. R. Stamenkovic, S. Pejovnik and N. M. Marković, *Nat. Mater.*, 2010, **9**, 998–1003.
87 Y.-H. Chung, S. J. Kim, D. Y. Chung, H. Y. Park, Y.-E. Sung, S. J. Yoo and J. H. Jang, *Chem. Commun.*, 2015, **51**, 2968–2971.
88 B. Hammer and J. K. Nørskov, *Adv. Catal.*, 2000, **45**, 71–129.
89 Y.-H. Chung, D. Y. Chung, N. Jung and Y.-E. Sung, *J. Phys. Chem. Lett.*, 2013, **4**, 1304–1309.
90 D. Li, C. Wang, D. Tripkovic, S. Sun, N. M. Marković and V. R. Stamenkovic, *ACS Catal.*, 2012, **2**, 1358–1362.
91 C. Koenigsmann, A. C. Santulli, K. Gong, M. B. Vukmirovic, W.-P. Zhou, E. Sutter, S. S. Wong and R. R. Adzic, *J. Am. Chem. Soc.*, 2011, **133**, 9783–9795.
92 B. S. Mun, C. Lee, V. Stamenkovic, N. M. Marković and J. Philip N Ross, *Phys. Rev. B: Condens. Matter Mater. Phys.*, 2005, **71**, 115420.
93 W.-p. Zhou, A. Lewera, R. Larsen, R. I. Masel, P. S. Bagus and A. Wieckowski, *J. Phys. Chem. B*, 2006, **110**, 13393–13398.
94 V. R. Stamenkovic, B. S. Mun, M. Arenz, K. J. J. Mayrhofer, C. A. Lucas, G. Wang, P. N. Ross and N. M. Marković, *Nat. Mater.*, 2007, **6**, 241–247.
95 V. R. Stamenkovic, B. Fowler, B. S. Mun, G. Wang, P. N. Ross, C. A. Lucas and N. M. Marković, *Science*, 2007, **315**, 493–497.
96 A. E. Russell and A. Rose, *Chem. Rev.*, 2004, **104**, 4613–4636.
97 S. Mukerjee, S. Srinivasan, M. P. Soriaga and J. McBreen, *J. Electrochem. Soc.*, 1995, **142**, 1409–1422.
98 L. Altmann, S. Kunz and M. Bäumer, *J. Phys. Chem. C*, 2014, **118**, 8925–8932.
99 W. Chen, S. W. Chen, F. Z. Ding, H. B. Wang, L. E. Brown and J. P. Konopelski, *J. Am. Chem. Soc.*, 2008, **130**, 12156–12162.

100 W. Chen, N. B. Zuckerman, X. W. Kang, D. Ghosh, J. P. Konopelski and S. W. Chen, *J. Phys. Chem. C*, 2010, **114**, 18146–18152.
101 X. Kang, N. B. Zuckerman, J. P. Konopelski and S. Chen, *Angew. Chem.*, 2010, **122**, 9686–9689.
102 X. W. Kang, N. B. Zuckerman, J. P. Konopelski and S. W. Chen, *J. Am. Chem. Soc.*, 2012, **134**, 1412–1415.
103 Z. Y. Zhou, X. W. Kang, Y. Song and S. W. Chen, *Chem. Commun.*, 2012, **48**, 3391–3393.
104 Z. Y. Zhou, X. W. Kang, Y. Song and S. W. Chen, *J. Phys. Chem. C*, 2012, **116**, 10592–10598.
105 G. Q. He, Y. Song, X. W. Kang and S. W. Chen, *Electrochim. Acta*, 2013, **94**, 98–103.
106 K. Liu, X. W. Kang, Z. Y. Zhou, Y. Song, L. J. Lee, D. Tian and S. W. Chen, *J. Electroanal. Chem.*, 2013, **688**, 143–150.
107 L. M. Chen, Y. Song, P. G. Hu, C. P. Deming, Y. Guo and S. W. Chen, *Phys. Chem. Chem. Phys.*, 2014, **16**, 18736–18742.
108 P. G. Hu, P. N. Duchesne, Y. Song, P. Zhang and S. W. Chen, *Langmuir*, 2015, **31**, 522–528.
109 L. M. Chen, P. G. Hu, C. P. Deming, W. Li, L. G. Li and S. W. Chen, *J. Phys. Chem. C*, 2015, **119**, 15449–15454.
110 P. Hu, L. Chen, C. P. Deming, X. Kang and S. Chen, *Angew. Chem., Int. Ed.*, 2016, **128**, 1477–1481.
111 Y. Peng, C. P. Deming and S. W. Chen, *ChemElectroChem*, 2016, **3**, 1219–1224.
112 Y. Peng, J. E. Lu, C. P. Deming, L. M. Chen, N. Wang, E. Y. Hirata and S. W. Chen, *Electrochim. Acta*, 2016, **211**, 704–710.
113 L. P. Hammett, *J. Am. Chem. Soc.*, 1937, **59**, 96–103.
114 C. Hansch, A. Leo and R. W. Taft, *Chem. Rev.*, 2002, **91**, 165–195.
115 Z.-Y. Zhou, X. Kang, Y. Song and S. Chen, *Chem. Commun.*, 2011, **47**, 6075–6077.
116 Z.-Y. Zhou, J. Ren, X. Kang, Y. Song, S.-G. Sun and S. Chen, *Phys. Chem. Chem. Phys.*, 2012, **14**, 1412–1417.
117 P. G. Hu, L. M. Chen, C. P. Deming, L. W. Bonny, H. W. Lee and S. W. Chen, *Chem. Commun.*, 2016, **52**, 11631–11633.
118 P. G. Hu, L. M. Chen, C. P. Deming, J. E. Lu, L. W. Bonny and S. W. Chen, *Nanoscale*, 2016, **8**, 12013–12021.
119 J. Wu, S.-X. Liu, A. Neels, F. Le Derf, M. Sallé and S. Decurtins, *Tetrahedron*, 2007, **63**, 11282–11286.
120 C.-P. Hsieh, H.-P. Lu, C.-L. Chiu, C.-W. Lee, S.-H. Chuang, C.-L. Mai, W.-N. Yen, S.-J. Hsu, E. W.-G. Diau and C.-Y. Yeh, *J. Mater. Chem.*, 2010, **20**, 1127–1134.
121 G. L. Eakins, J. S. Alford, B. J. Tiegs, B. E. Breyfogle and C. J. Stearman, *J. Phys. Org. Chem.*, 2011, **24**, 1119–1128.
122 L. Zöphel, V. Enkelmann and K. Müllen, *Org. Lett.*, 2013, **15**, 804–807.
123 K. Liu, Y. Song and S. Chen, *Nanoscale*, 2014, **7**, 1224–1232.
124 C. P. Deming, A. Zhao, Y. Song, K. Liu, M. M. Khan, V. M. Yates and S. W. Chen, *ChemElectroChem*, 2015, **2**, 1719–1727.
125 G. Q. He, Y. Song, K. Liu, A. Walter, S. Chen and S. W. Chen, *ACS Catal.*, 2013, **3**, 831–838.
126 Y. Song and S. W. Chen, *ACS Appl. Mater. Interfaces*, 2014, **6**, 14050–14060.
127 K. Liu, Y. Song and S. W. Chen, *Int. J. Hydrogen Energy*, 2016, **41**, 1559–1567.
128 C. P. Deming, R. Mercado, V. Gadiraju, S. W. Sweeney, M. Khan and S. W. Chen, *ACS Sustainable Chem. Eng.*, 2015, **3**, 3315–3323.
129 C. P. Deming, R. Mercado, J. E. Lu, V. Gadiraju, M. Khan and S. W. SChen, *ACS Sustainable Chem. Eng.*, 2016, **4**, 5280–6589.
130 K. Song, Z. Zou, D. Wang, B. Tan, J. Wang, J. Chen and T. Li, *J. Phys. Chem. C*, 2016, **120**, 2187–2197.
131 L. Guo, W.-J. Jiang, Y. Zhang, J.-S. Hu, Z.-D. Wei and L.-J. Wan, *ACS Catal.*, 2015, **5**, 2903–2909.
132 Q. Wang, L. Wang, Z. Tang, F. Wang, W. Yan, H. Yang, W. Zhou, L. Li, X. Kang and S. Chen, *Nanoscale*, 2016, **8**, 6629–6635.
133 J. Lu, W. Zhou, L. Wang, J. Jia, Y. Ke, L. Yang, K. Zhou, X. Liu, Z. Tang, L. Li and S. Chen, *ACS Catal.*, 2016, **6**, 1045–1053.
134 L. Zhang and Z. Xia, *J. Phys. Chem. C*, 2011, **115**, 11170–11176.
135 W. Ding, Z. D. Wei, S. G. Chen, X. Q. Qi, T. Yang, J. S. Hu, D. Wang, L. J. Wan, S. F. Alvi and L. Li, *Angew. Chem., Int. Ed.*, 2013, **52**, 11755–11759.
136 D. H. Guo, R. Shibuya, C. Akiba, S. Saji, T. Kondo and J. Nakamura, *Science*, 2016, **351**, 361–365.
137 H. B. Yang, J. Miao, S.-F. Hung, J. Chen, H. B. Tao, X. Wang, L. Zhang, R. Chen, J. Gao, H. M. Chen, L. Dai and B. Liu, *Sci. Adv.*, 2016, **2**, e1501122.
138 H. Kim, K. Lee, S. I. Woo and Y. Jung, *Phys. Chem. Chem. Phys.*, 2011, **13**, 17505–17510.
139 A. L. Shen, Y. Q. Zou, Q. Wang, R. A. W. Dryfe, X. B. Huang, S. Dou, L. M. Dai and S. Y. Wang, *Angew. Chem., Int. Ed.*, 2014, **53**, 10804–10808.
140 C. Tang, H.-F. Wang, X. Chen, B.-Q. Li, T.-Z. Hou, B. Zhang, Q. Zhang, M.-M. Titirici and F. Wei, *Adv. Mater.*, 2016, **28**, 6845–6851.
141 K. Gong, F. Du, Z. Xia, M. Durstock and L. Dai, *Science*, 2009, **323**, 760–764.
142 D. R. Lide, *CRC handbook of chemistry and physics: a ready-reference book of chemical and physical data*, CRC Press, Boca Raton, Fla, 85th edn, 2004.
143 X. J. Liu, L. G. Li, W. J. Zhou, Y. C. Zhou, W. H. Niu and S. W. Chen, *ChemElectroChem*, 2015, **2**, 803–810.
144 J. Liu, L. G. Li, W. H. Niu, N. Wang, D. K. Zhao, S. B. Zeng and S. W. Chen, *ChemElectroChem*, 2016, **3**, 1116–1123.
145 W. H. Niu, L. G. Li, J. Liu, N. Wang, W. Li, Z. H. Tang, W. J. Zhou and S. W. Chen, *Small*, 2016, **12**, 1900–1908.
146 X. J. Liu, S. Z. Zou and S. W. Chen, *Nanoscale*, 2019, **8**, 19249–19255.
147 W. H. Niu, L. G. Li, N. Wang, S. B. Zeng, J. Liu, D. K. Zhao and S. W. Chen, *J. Mater. Chem. A*, 2016, **4**, 10820–10827.
148 X. Sun, Y. Zhang, P. Song, J. Pan, L. Zhuang, W. Xu and W. Xing, *ACS Catal.*, 2013, **3**, 1726–1729.

149 X. Wang, G. Sun, P. Routh, D.-H. Kim, W. Huang and P. Chen, *Chem. Soc. Rev.*, 2014, **43**, 7067–7098.
150 Y. C. Wang, Y. J. Lai, L. Song, Z. Y. Zhou, J. G. Liu, Q. Wang, X. D. Yang, C. Chen, W. Shi, Y. P. Ren, M. Rauf and S. G. Sun, *Angew. Chem., Int. Ed.*, 2015, **54**, 9907–9910.
151 L. Yang, S. Jiang, Y. Zhao, L. Zhu, S. Chen, X. Wang, Q. Wu, J. Ma, Y. Ma and Z. Hu, *Angew. Chem., Int. Ed.*, 2011, **123**, 7270–7273.
152 Z.-W. Liu, F. Peng, H.-J. Wang, H. Yu, W.-X. Zheng and J. Yang, *Angew. Chem., Int. Ed.*, 2011, **123**, 3315–3319.
153 S. Wang, D. Yu, L. Dai, D. W. Chang and J.-B. Baek, *ACS Nano*, 2011, **5**, 6202–6209.
154 S. Wang, D. Yu and L. Dai, *J. Am. Chem. Soc.*, 2011, **133**, 5182–5185.
155 M. Zhang, W. Yuan, B. Yao, C. Li and G. Shi, *ACS Appl. Mater. Interfaces*, 2014, **6**, 3587–3593.